Proceedings of the 50th International School & Conference on the Physics of Semiconductors

Low Temperature Weak Anti-Localization Effect in the GeTe and SnTe Epitaxial Layers

A. Khaliq*, P. Dziawa, R. Minikaev, M. Arciszewska, A. Avdonin, B. Brodowska and L. Kilański

Institute of Physics, Polish Academy of Sciences, al. Lotnikow 32/46, PL-02668 Warsaw, Poland

Doi: 10.12693/APhysPolA.142.657 *e-mail: akhaliq@ifpan.edu.pl

IV–VI semiconductors possess intriguing multifunctional characteristics, such as topological surface states, ferroelectricity at room temperature, and giant Rashba spin-splitting, giving them the potential for next-generation spintronic applications. In this work, we are presenting the epitaxially grown layers α-GeTe and SnTe, their structural and high field magnetotransport results. The crystal structure of α-GeTe preserves the rhombohedral symmetry ($R3m$) below $T \approx 720$ K manifesting ferroelectric polarization, whereas SnTe holds the cubic symmetry (Fm-$3m$) above $T \approx 80$ K. The results of the variable temperature in the range $4.3 \leq T \leq 300$ K show a weakly dependent charge concentration, i.e., $p(T) = 0.1 \times 10^{21}$ cm^{-3} for SnTe and $p(T) = 0.7 \times 10^{21}$ cm^{-3} for α-GeTe layers. Likewise, the hole mobility $\mu_h(T)$ remains almost constant in the range $4.3 \leq T \leq 15$ K and changes to a metallic-like behavior when $T \geq 15$ K. Furthermore, the high field magnetoresistance $\rho_{xx}(B)$ graphs of SnTe layers, measured between $-13 \leq B \leq 13$ T, demonstrate a prominent weak anti-localization effect below $T = 3$ K and when $|B| \leq 0.3$ T. However, the weak anti-localization effect disappears at $T = 4.2$ K for both the α-GeTe and SnTe epitaxial layers. Similarly, the $\rho_{xx}(B)$ graphs of α-GeTe show a small effect only at the lowest temperature measured $T = 1.6$ K. The calculated prefactor value $\alpha = -14$, obtained by fitting the $\Delta\sigma_{xx}(B)$ graphs with the Hikami–Larkin–Nagaoka model, indicates the bulk transport system in SnTe.

topics: IV–VI semiconductors (SCs), weak anti-localization effect, bulk conductivity

1. Introduction

Narrow bandgap IV–VI compound semiconductors (SCs) have witnessed a diverse range of new discoveries such as topological edge states [1], quantum Hall effect [2], multi-channel transport in quantum wells [3], efficient high-temperature thermoelectric capabilities [4] and the intimate link between ferroelectric polarization and spin orientation [5]. With regard to topological features, SnTe with a direct band gap of ~ 0.18 eV [6] has been rigorously studied and categorized as a bulk insulator although it consists of metallic surface states. The topological crystalline insulator — SnTe — was first theoretically predicted by Hsieh et al. [7], in 2012 which has garnered plentiful of research since then. The robust metallic surface states are believed to originate from the intrinsic spin–orbit interaction in topological materials that are protected by high symmetry planes (111), (110), and (100) [3]. Later, the existence of topological surface states in SnTe was experimentally verified using the angle-resolved photoemission spectroscopy (ARPES) technique, whereas its topological features were also detected via magnetoresistance measurements [1, 8]. SnTe based materials also showed exciting thermoelectric performance at room temperature with the thermoelectric figure of merit $ZT \sim 0.3$ [4].

Also, α-GeTe offers many striking functional properties that are crucial in terms of the implementation of spintronic device. Among them, the existence of high-temperature ferroelectricity below $T \approx 720$ K suggests its suitability for non-volatile memory applications [5]. Similarly, recent theoretical prediction and experimental demonstration of the ferroelectric control of spin-texture in α-GeTe indicate that this simple compound could be a platform yielding rich spintronic functionality [9, 10]. The presence of a Rashba spin splitting in α-GeTe provides spin-degrees of freedom that can be exploited in semiconductor logic applications [9].

The study of electrical transport of SCs at low temperature and high magnetic field yield intriguing physical phenomena, such as Landau quantization, integral and fractional quantum Hall effect [11]. Among them, the occurrence of a low-temperature cusp-like shape in magnetoresistance has been previously shown for quantum wells [3], thin films [12] and bulk materials [13]. Such a physical effect is broadly categorized as either

weak localization (WL) or weak anti-localization (WAL), which depends on the sign of magnetoresistance [14]. In previous works, the localization effects have been attributed to quantum coherent transport of charge carriers. Singh et al. [8] observed WAL in nanocrystalline quasi two-dimensional SnTe. Similarly, Akiyama et al. [15] produced highly oriented monocrystalline SnTe thin films that manifested a similar WAL effect. Likewise, the WAL effect was also detected in a 30 nm SnTe quantum well by Castro et al. [3]. This suggests that IV–VI SCs with a narrow bandgap show localization phenomena in diverse form of physical shapes and dimensions.

In this work, we discuss the results of magnetotransport of binary alloys α-GeTe and SnTe in the applied magnetic field range $-13 \leq B \leq 13$ T. The epitaxially grown layers have a thickness ≈ 470 nm. It is important for the electrical transport part that in our layers the charge (hole) carrier concentration $p(T)$ [cm^{-3}] exhibits an astonishingly weak temperature dependence from $T = 4.2$ K to $T = 300$ K. From the magnetoresistance results, the SnTe layers show a pronounced valley-like shape when $|B| \leq 0.3$ T and $T \leq 3$ K. We further demonstrate that this cusp-like shape originates due to the WAL effect by analyzing the magnetoconductivity graphs with the Hikami–Larkin–Nagaoka equation.

2. Results and discussion

The room temperature crystal structure of α-GeTe and SnTe was measured using high resolution X-ray diffractometer (HRXRD) facilitated with Cu K_{α_1} radiation of a wavelength $\lambda = 1.5406$ Å. Our diffraction results show that α-GeTe has a rhombohedral ($R3m$) crystal structure, with the powder diffraction file (*.pdf) no. 47-1079 (Inorganic Crystal Structure Database, ICSD collection code 56038) [16]. In comparison to α-GeTe, the room temperature crystal symmetry of SnTe layers revealed a cubic (Fm-$3m$) phase with file (*.pdf) no. 46-1210 (Inorganic Crystal Structure Database, ICSD Collection Code 52489) [17]. Since the paraelectric to ferroelectric phase transition occurs at $T \approx 720$ K and $T \approx 80$ K for GeTe and SnTe crystals, respectively, both crystal systems are in the ferroelectric regime at low temperatures used in magnetotransport measurements. Similarly, the layers' thickness ($t \approx 470$ nm) for both layers was investigated using a scanning electron microscope (SEM).

The electrical transport measurements of the layers were executed in order to examine the features of charge concentration and mobility of the α-GeTe and SnTe layers. Using the six contacts direct current (DC) method in the temperature range $4.3 \leq T \leq 300$ K, measurements were performed at a direct current $I = 1$ mA and a magnetic field $B = 1.4$ T. In Fig. 1, graphs of the hole concentration $p(T)$ and the mobility $\mu_h(T)$

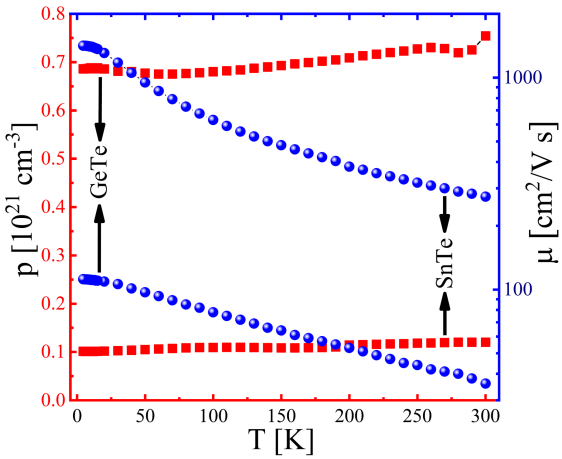

Fig. 1. Temperature dependence of the hole carrier concentration $p(T)$ of α-GeTe and SnTe epitaxial layers denoted by the left vertical axis. The mobility $\mu(T)$ graphs are indicated by the right vertical axis. The horizontal axis between $4.3 \leq T \leq 300$ K is same for both quantities.

are presented. For GeTe layers, the comparatively high hole concentration remains almost constant ($p(T) \simeq 0.7 \times 10^{21}$ cm^{-3}) in the whole temperature range. The same observation holds for the SnTe sample ($p(T) \simeq 0.1 \times 10^{21}$ cm^{-3}), which shows a 7-fold smaller value compared to the α-GeTe layer. It is obvious from Fig. 1 that the $p(T)$ graphs of both α-GeTe and SnTe manifest a nearly independent temperature behavior. The temperature-independent behavior of charge carriers illustrates that binary alloys belong to degenerate semiconductors. Furthermore, the variation of electrical mobility with the temperature, $\mu_h(T)$, is presented in Fig. 1 in the same temperature range.

For the SnTe layers, in the temperature regime $4.3 \leq T \leq 15$ K, $\mu_h(T) \approx 1400$ cm^2 V^{-1} s^{-1}, which is about fourteen times larger than $\mu_h(T) \approx 100$ cm^2 V^{-1} s^{-1} for the α-GeTe layer. Note that up to room temperature the value of $\mu_h(T)$ for the SnTe sample still has a comparatively higher value of ≈ 270 cm^2 V^{-1} s^{-1}. In the low-temperature regime, the $\mu_h(T)$ graphs for both samples remain almost constant between $4.3 \leq T \leq 15$ K. However, the mobility values decrease as a function of temperature for $T \geq 15$ K. The decrease in $\mu(T)$ for the α-GeTe layers exhibits an almost constant slope, whereas the graph for SnTe presents an accelerated decline until $T = 130$ K. When $T \geq 130$ K, the $\mu(T)$ behavior of SnTe is similar to that of GeTe expressing a sluggish decrease. The decline in the hole mobility in the range $T = 15$–300 K can be illustrated as the temperature range in which the lattice vibration scatterings dominate in the studied layered systems [18]. The phonon scattering causing a decline of the $\mu_h(T)$ values is a typical physical mechanism responsible for such decreasing behavior of electrical mobility.

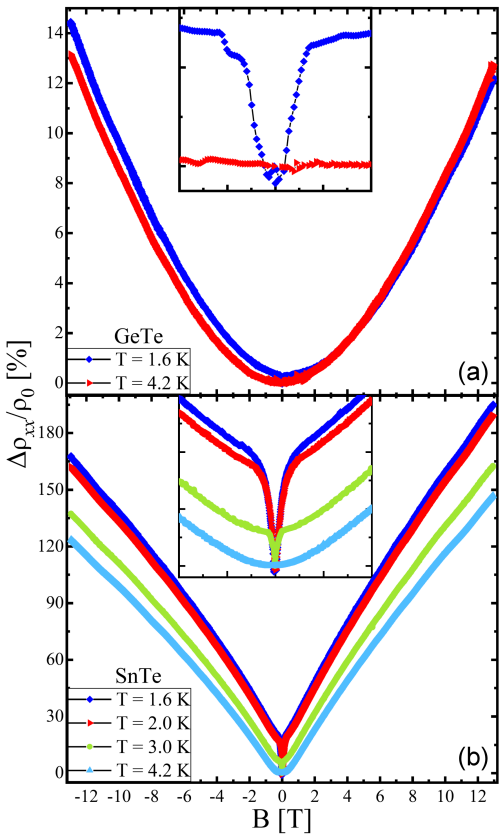

Fig. 2. (a) The magnetic field-dependent longitudinal resistivity $\rho_{xx}(B)$ of the α-GeTe layers at $T = 1.6$ K and 4.2 K. The inset of (a) shows a cut of $\rho_{xx}(B)$ when $|B| \leq 0.1$ T. (b) The graphs of $\rho_{xx}(B)$ of the SnTe samples in the low temperature range $1.6 \leq T \leq 4.2$ K. The inset presents an amplified image of (b) when $|B| \leq 0.2$ T.

In addition to temperature-dependent electrical transport, this work adds an analysis of magnetotransport measured via superconducting magnet in the range $-13 \leq B \leq 13$ T in order to study the charge scattering. This part of the measurement includes the magnetic field-dependent longitudinal resistivity $\rho_{xx}(B)$ and the magnetic field-dependent transverse (Hall) resistivity $\rho_{xy}(B)$. We used the six-probe method to measure magnetotransport. The graphs of $\rho_{xx}(B)$ of the α-GeTe and SnTe layers are presented in Fig. 2a and b, respectively. The magnetoresistance values presented here have been normalized to the zero field resistivity ρ_0 using the relation $\Delta\rho_{xx}/\rho_{xx}(0) = \rho_{xx}(B) - \rho_{xx}(B = 0)/\rho_{xx}(B = 0)$. For the α-GeTe layers, the $\Delta\rho_{xx}/\rho_0$ graph measured at the lowest accessible temperature $T = 1.6$ K manifests a valley-like shape around the zero magnetic field. As the temperature increases, the magnitude of the valley vanishes for $T \geq 2$ K; the $\Delta\rho_{xx}/\rho_0$ graph is shown at $T = 4.2$ K expressing ordinary behavior. Figure 2b shows the $\Delta\rho_{xx}/\rho_0$ results of SnTe layers measured under the same conditions. Compared to Fig. 2a, the valley-shape in the SnTe layers is relatively prominent and rises to $\Delta\rho_{xx}/\rho_0 = 20\%$ at $T = 1.6$ K as opposed to 0.27% for the α-GeTe. The presence of the valley persists until $T \leq 3$ K, then its magnitude decreases at elevated temperatures and disappears at $T = 4.2$ K (see Fig. 2b). Moreover, as the temperature is raised, the magnitude of $\rho_{xx}(B)$ in Fig. 2a, b reduces. Therefore, the graphs of $\Delta\rho_{xx}/\rho_0$ can be categorized as a low-field parabolic region and a high-field linear part. Also, the temperature dependence of the low field region is prominent, while the high field part shows negligible variation, indicating the quantum nature of the valley-like shape around the zero field regime.

A sharp valley in $\Delta\rho_{xx}/\rho_0$ around the zero field has been previously observed for different material systems such as nanocrystalline SnTe [8], SnTe quantum wells [3], topologically nontrivial semimetal LuPdBi [19] and Cu-doped Bi_2Se_3 films [20]. In the above few of the many magnetotransport studies, a sharp dip or valley around the zero field was analyzed and attributed to the weak anti-localization effect. The observed valley in our samples exhibits similar signatures of the WAL effect, which arises from quantum interference of time-reversed loops of scattering charge carriers. In the quantum diffusive regime in which a dip in magnetoresistance near the zero field occurs, the condition $\ell_\varphi \gg \ell$ holds for the WAL effect, where ℓ characterizes the average distance traveled by the charge carrier before its momentum changes, and ℓ_φ is the phase coherence length of the diffusive carriers [14]. In such a regime, the charge carriers maintain their phase associated with the wave function even after encountering several scatterings. In order to analyze the WAL regime in the current samples and investigate its origin, we fit the magnetoconductivity $\Delta\sigma_{xx}(B)$ at different temperatures with the Hikami–Larkin–Nagaoka (HLN) model [3] accordingly

$$\Delta\sigma_{xx}(B) = -\frac{e^2\alpha}{2\pi^2\hbar}\left[\ln\left(\frac{B_\varphi}{B}\right) - \psi\left(\frac{1}{2}+\frac{B_\varphi}{B}\right)\right]. \tag{1}$$

In (1), α is the prefactor indicating the number of coherent conduction channels, e is the elementary electronic charge, $B_\varphi = \hbar/(4e\ell_\varphi^2)$ is the characteristic magnetic field, $\hbar$ is Planck's constant, ℓ_φ is the phase coherence length, and $\psi(\cdot)$ represents the digamma function. Subsequently, the fitting parameters α and ℓ_φ yield the values of prefactor α and the phase coherence length, respectively.

In this section, we discuss the origin of the conductive channels and the quantum diffusive features of charge carriers that cause the WAL effect. The valley-like shapes presented in Fig. 2 are further analyzed after fitting with (1). But first the $\Delta\rho_{xx}$ graphs had to be converted into the magnetoconductivity (MC) $\Delta\sigma_{xx}(B)$ to get graphs appropriate for the HLN model, see Fig. 3. The MC fit was obtained around the zero field region deduced from Fig. 2, which represents the WAL effect

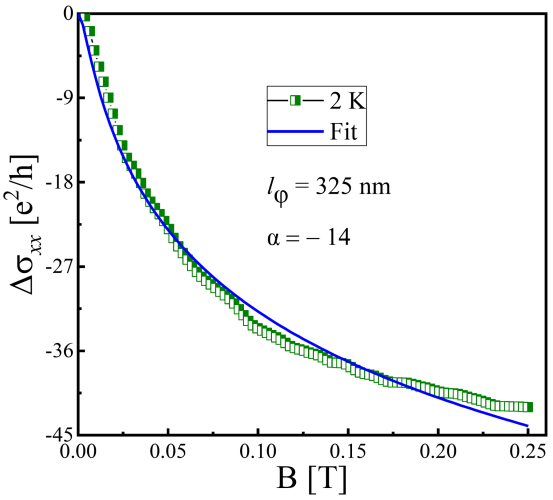

Fig. 3. The obtained magnetoconductivity $\Delta\sigma_{xx}(B)$ graph of the SnTe layer measured at $T = 2$ K. The half-filled symbols represent experimental results, while the solid line denotes the fit to the HLN model. The phase coherence length ℓ_φ and prefactor α values are shown; they were obtained after fitting the $\Delta\sigma_{xx}(B)$ graph to (1).

about $|B| \leq 0.3$ T. The decrease in the MC values is sharp at small magnetic field values ($B \leq 0.1$ T), which is attributed to the WAL effect occurring in the SnTe layers [21]. Such an effect is quantum in nature and originates from the interference of the wave functions of the charge carriers. The WAL effect arises as a quantum correction to the classical nature of conductivity. In topological insulators such as SnTe, quantum correction to classical conductivity at low field can occur both due to the strong spin–orbit interaction in the bulk state and the topological edge states [19].

As presented in Fig. 3, the $\Delta\sigma_{xx}(B)$ graph at $T = 2$ K and the corresponding fit are shown below $B = 0.3$ T. The obtained values of the phase coherence length value and the prefactor were $\ell_\varphi = 325$ nm and $\alpha = -14$, respectively, and were used as the fitting parameters, see (1). The value of ℓ_φ was calculated from the dephasing field using the relation $B_\varphi = \hbar/(4e\ell_\varphi^2)$. The ℓ_φ value obtained for our layers is similar to the value in previously studied systems, such as the magnetron sputtered Bi_2Te_3 thin films [12], single crystal LuPtSb [18] and the topological insulator Bi_2Te_3 [22]. However, our value is substantially bigger than the values obtained for very thin layers, e.g. single-crystalline Bi_2Se_3 nanoribbons [23] and epitaxially grown Bi_2Se_3 thin films [24]. In order to carefully understand the origin of the WAL effect, it is important to analyze the value of the prefactor α. For typical two-dimensional conducting systems, α yields the value of -1, which indicates the number of coherent conducting surface channels in the material, with each transport channel contributing $\alpha = -0.5$ [15, 18]. The calculated value for the SnTe layers in this study, $\alpha = -14$, is considerably greater than the established theoretical values. A similarly large value, i.e., $\alpha = -16.7$, was obtained by Hou et al. [13] for bulk black phosphorus. This large deviation in the value of the prefactor was attributed to the presence of a three-dimensional bulk transport system [18, 25]. The layers studied in this work have a thickness of $t \approx 470$ nm, which presents a three-dimensional transport system in comparison to other works referenced. Therefore, based on the dimensions of the epitaxial layers and the calculated value of the prefactor α, we deduce that the WAL effect originates from the bulk conductive channels guided by spin–orbit interactions.

3. Conclusions

Electrical and magnetotransport studies of the epitaxial layers of α-GeTe and SnTe SCs of a thickness $t \approx 470$ nm were performed. The hole concentration in both compounds was obtained $\sim 10^{21}$ cm^{-3}, exhibiting behavior almost independent of temperature from $T = 4.3$ K to 300 K. Similarly, the electrical mobility $\mu_h(T)$ manifests a constant manner in the temperature range $4.3 \leq T \leq 15$ K, however, it gradually decreases at elevated temperatures. Such a trend could have arisen from the dominant phonon scatterings caused by lattice vibrations. The longitudinal magnetoresistance $\Delta\rho_{xx}/\rho_0$ results illustrate a valley-like shape at low temperatures and weak magnetic fields. This effect was described by the HLM model using (1), which yielded a considerably large value of the prefactor α used as the fitting parameter. Finally, we conclude that detailed analyses of the quantum correction to conductivity signify that the WAL effect is present, and the bulk transport channels dominate in the semiconducting system.

Acknowledgments

The research was financed by the National Science Centre, Poland, under the project number 2018/30/E/ST3/00309.

References

[1] Y. Tanaka, Z. Ren, T. Sato, K. Nakayama, S. Souma, T. Takahashi, K. Segawa, Y. Ando, *Nat. Phys.* **8**, 800 (2012).

[2] V.A. Chitta, W. Desrat, D.K. Maude, B.A. Piot, N.F. Oliveira, Jr., P.H.O. Rappl, A.Y. Ueta, E. Abramof, *Phys. Rev. B* **72**, 195326 (2005).

[3] S. de Castro, B. Kawata, G.R.F. Lopes, P.H. de O. Rappl, E. Abramof, M.L. Peres, *Appl. Phys. Lett.* **120**, 203102 (2022).

[4] U.S. Shenoy, D.K. Bhat, *J. Mater. Chem. C*, **8**, 2036 (2020).

[5] D.D. Sante, P. Barone, R. Bertacco, S. Picozzi, *Adv. Mater.* **25**, 509 (2013).

[6] M.V. Kovalenko, W. Heiss, E.V. Shevchenko, J.S. Lee, H. Schwinghammer, A.P. Alivisatos, D.V. Talapin, *J. Am. Chem. Soc.* **129**, 11354 (2007).

[7] T.H. Hsieh, H. Lin, J. Liu, W. Duan, A. Bansil, L. Fu, *Nat. Commun.* **3**, 982 (2012).

[8] S. Singh, H. Afzal, V. Kaushik, S. Kumar, P. Behera, R. Venkatesh, *Langmuir* **38**, 3122 (2022).

[9] S. Picozzi, *Front. Phys.* **2**, 1 (2014).

[10] C. Rinaldi, S. Varotto, M. Asa et al., *Nano Lett.* **18**, 2751 (2018).

[11] D. C. Tsui, *Physica B* **164**, 59 (1990).

[12] A. Pilidi, Th. Speliotis and G. Litsardakis, *J. Magn. Magn. Mater.* **511**, 166971 (2020).

[13] Z. Hou, C. Gong, Y. Wang et al., *J. Phys. Condens. Matter* **30**, 085703 (2018).

[14] H. Z. Lu and S. Q. Shen, *Proc. SPIE* **9167**, 91672E (2014).

[15] R. Akiyama, K. Fujisawa, T. Yamaguchi, R. Ishikawa, S. Kuroda, *Nano Res.* **9**, 490 (2016).

[16] T.K. Chattopadhyay, J.X. Boucherle, H.G. von Schnering, *J. Phys. C Solid State Phys.* **20**, 1431 (1987).

[17] E.I. Rogacheva, G.V. Gorne, S.A. Laptev, A.V. Arinkin, T.B. Vesiene, *Neorganicheskie Materialy* **22**, 41 (1986).

[18] Z. Hou, Y. Wang, G. Xu, X. Zhang, E. Liu, W. Wang, Z. Liu, X. Xi, W. Wang, G. Wu, *Appl. Phys. Lett.* **106**, 102102 (2015).

[19] G. Xu, W. Wang, X. Zhang, Y. Du, E. Liu, S. Wang, G. Wu, Z. Liu, X.X. Zhang, *Sci. Rep.* **4**, 5709 (2014).

[20] Y. Takagaki, B. Jenichen, U. Jahn, M. Ramsteiner, K.-J. Friedland, *Phys. Rev. B* **85**, 115314 (2012).

[21] S. Hikami, A.I. Larkin, Y. Nagaoka, *Prog. Theor. Phys.* **63**, 707 (1980).

[22] H.T. He, G. Wang, T. Zhang, I.K. Sou, G.K.L. Wong, J.N. Wang, H.Z. Lu, S.Q. Shen, F.C. Zhang, *Phys. Rev. Lett.* **106**, 166805 (2011).

[23] H.L. Peng, K.J. Lai, D.S. Kong, S. Meister, Y.L. Chen, X.L. Qi, S.C. Zhang, Z.X. Shen, Y. Cui, *Nat. Mater.* **9**, 225 (2010).

[24] J. Chen, H.J. Qin, F. Yang et al., *Phys. Rev. Lett.* **105**, 176602 (2010).

[25] J. Shen, Y. Xie, J.J. Cha, *Nano Lett.* **15**, 3827 (2015).